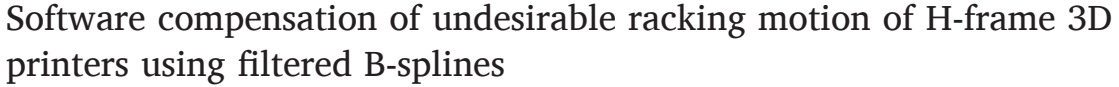
Contents lists available at ScienceDirect

Additive Manufacturing

journal homepage: www.elsevier.com/locate/addma



Research Paper



Nosakhare Edoimioya, Keval S. Ramani, Chinedum E. Okwudire

Department of Mechanical Engineering, University of Michigan, Ann Arbor, MI 48109, USA



Keywords: H-Frame H-Bot FFF 3D printing Filtered B-splines Feedforward vibration control



ABSTRACT

The H-frame (also known as H-Bot) architecture is a simple and elegant two-axis parallel positioning system used to construct the XY stage of 3D printers. It holds potential for high speed and high dynamic performance due to the use of frame-mounted motors that reduce the moving mass of the printer while allowing for the use of (heavy) higher torque motors. However, the H-frame's dynamic accuracy is limited during high-acceleration and high-speed motion due to racking – i.e., parasitic torsional motions of the printer's gantry due to a force couple. Mechanical solutions to the racking problem are either costly or detract from the simplicity of the H-frame. In this paper, we introduce a feedforward software compensation algorithm, based on the filtered B-splines (FBS) method, that rectifies errors due to racking. The FBS approach expresses the motion command to the machine as a linear combination of B-splines. The B-splines are filtered through an identified model of the machine dynamics and the control points of the B-spline based motion command are optimized such that the tracking error is minimized. To compensate racking using the FBS algorithm, an accurate frequency response function of the racking motion is obtained and coupled to the H-frame's and y-axis dynamics with a kinematic model. The result is a coupled linear parameter varying model of the H-frame that is utilized in the FBS framework to compensate racking. An approximation of the proposed racking compensation algorithm, that decouples the x- and y-axis compensation, is developed to significantly improve its computational efficiency with almost no loss of compensation accuracy. Experiments on an H-frame 3D printer demonstrate a 43% improvement in the shape accuracy of a printed part using the proposed algorithm compared to the standard FBS approach without racking compensation. The proposed racking compensation algorithm can be used in-conjunction with mechanical solutions, or as a stand-alone solution, to improve the performance of H-frame architectures.

1. Introduction

Fused filament fabrication (FFF) 3D printers, which represent approximately 70% of the 3D printing market [1], manufacture parts by extruding material from a heated nozzle onto a bed, with the help of motion systems that move the nozzle and bed. The standard choice for motion systems of FFF 3D printers is the so-called serial stack architecture, which generates motion using independent (i.e., decoupled) actuators for each axis, and typically requires one of the axes and its associated motor(s) to be "stacked" on another axis. This stacking leads to high inertial loads and motion friction, which limit the dynamic accuracy and the available torque during high-speed motions. Although the serial stack architecture is still a popular choice, less conventional motion systems such as the H-frame [2], delta [3], and Core XY [4] architectures are designed using stationary motors to reduce the moving mass of the end-effector, allowing for increased dynamic accuracy and motion speed.

The H-frame architecture, as seen in Fig. 1(a), has a simple parallel axis design that consists of two motors mounted to the frame of the 3D printer, which are connected to the end-effector through a single timing belt. Translational motion in the x- and y-axis of the end-effector is generated via the rotational motion of the frame-mounted motors, which is transmitted by a timing belt and pulley configuration [2,5,6]. Since the motors are stationary, high-power (and, typically, heavy) motors can be utilized to achieve high-speed and high-precision motion without increasing the moving mass of the printer. For this reason, the H-frame architecture has been used in several 3D printers, such as the Stratasys Mojo [7], MakerBot Replicator Z18 [8], Creality Ender 4 [9], and MIT's Fast FFF [10] 3D printers. Using the H-frame as one of several improvements to conventional FFF 3D printers, Go et al. [10]

^{*} Correspondence to: 2656 G.G. Brown Building, 2350 Hayward Street, Ann Arbor, MI 48109, USA. E-mail addresses: nosed@umich.edu (N. Edoimioya), ksramani@umich.edu (K.S. Ramani), okwudire@umich.edu (C.E. Okwudire).

Fig. 1. (a) The H-frame architecture with stationary motors labeled M1 and M2 and the timing belt and pulley configuration that transmits rotational motion to XY translational motion of the gantry and end-effector; (b) Unbalanced forces, F, that cause racking—parasitic torsional motions—of the gantry.

demonstrated 5–10 times improvements in build rate using the Fast FFF printer compared to several printers of the same class. However, parts printed with H-frame 3D printers suffer from quality defects caused by parasitic error motions due to "racking" [4]: when the motors are commanded to rotate in the same direction, corresponding to *x*-axis motion of the end-effector, a force couple (pure moment) is imposed on the gantry (Fig. 1(b)) which, depending on the speed, may create large enough errors to distort the part shape. The magnitude of these errors also depends on the end-effector's location along the *x*-axis, indicating a parameter varying system [4].

Racking errors can be mitigated with mechanical solutions such as a rigid linear guideway design or adding counterweights to offset the racking, which add additional cost and weight to the gantry. A lower-cost option, that does not add weight to the gantry, is to design a modified configuration, such as the two-belt Core XY architecture [4], which ensures the forces on the gantry do not create a force couple. However, the Core XY and similar designs can be significantly more complex than the H-frame's design, and difficult to manufacture. Additionally, other sources of error may surface, such as the errors created on the Core XY when the two belts are not equally tensioned [4].

Conversely, software compensation (i.e., feedback and/or feedforward control algorithms) can be used to reduce or eliminate racking errors, often without need to modify the mechanical architecture of the printer. Although useful in a variety of applications, feedback (FB) control, which depends on sensing to correct errors, is impractical for racking compensation for the following reasons [6,11]: (1) It is not applicable to a wide range of 3D printers that are stepper motor-controlled in the open-loop (i.e., they have no position sensors); (2) the position sensors available on some 3D printers are motor-mounted, hence cannot sense racking at the end-effector; and (3) adding sensors that can sense racking at the end-effector will lead to non-collocated control systems that are prone to instability [12].

The challenges of FB control can be mitigated via feedforward (FF) control, which compensates errors using a model of the controlled system as opposed to sensing. Feedforward control has been shown to improve motion accuracy in a host of manufacturing applications, including 3D printing [13–21]. A popular FF control approach for reducing motion errors is called smooth command generation [22] where motion commands are generated to have little to no high-frequency content by using, for example, low-pass filters [23] and jerk-limited [24] trajectories. However, the attenuated high-frequency

content of smooth command generation implies loss of motion speed, which adversely affects productivity [15]. Additionally, smooth command generation methods are sub-optimal because motion commands are not generated with knowledge of the machine's dynamics [25]. Hence, conservative acceleration and jerk limits are often adopted in practice since there is no clear understanding of how to select the limits to achieve a desired performance metric [26]. Input shaping [27-29], another popular FF control method, eliminates vibration errors through destructive interference by commanding a series of impulses that are equal in magnitude but opposite in phase to the vibration errors of the system. A major limitation of input shaping is that it introduces time delays between the desired and actual motions, leading to large tracking/contouring errors and reduction of productivity [30]. Therefore, while it works well for point-to-point motions, it exhibits poor performance for the tracking/contouring motions prevalent in most AM applications. Another class of FF control methods is known as model-inversion based FF control. Methods in this class compensate motion errors by using the inverse of the motion system's dynamics to pre-filter motion commands. Model inversion-based FF control methods do not introduce time delays and can theoretically lead to perfect compensation of motion errors [31]. In practice, perfect compensation is difficult to achieve due to modeling errors [32] and the prevalence of nonminimum phase (or unstable) zeros, which become unstable poles after inversion. Hence, approximate model inversion-based FF controllers are employed, several of which are available, as discussed extensively in [31,33,34]. Of the available methods, the filtered basis functions (FBF) approach has been shown to be versatile, compared to others, regarding its applicability to any linear system dynamics [13,14, 35-38]. The FBF approach expresses motion commands as a linear combination of basis functions, forward filters the basis functions using the plant dynamics, and calculates the coefficients of the basis functions such that motion errors are minimized. A version of FBF commonly used for controlling manufacturing machines is the filtered B-splines (FBS) method [13-15,32,35], where B-splines are selected as the basis functions because they are amenable to the lengthy motion trajectories common in manufacturing. The FBS method has been used to reduce the printing time of serial stack FFF 3D printers by up to 54% without sacrificing print quality, by compensating vibration-induced errors [13, 15.16]. However, the standard implementation of the FBS method used in the aforementioned studies is not directly applicable to the compensation of racking in H-frame 3D printers because it assumes that the printer dynamics is linear time invariant (LTI) and decoupled, whereas racking dynamics is linear parameter varying (LPV) and coupled.

Therefore, to enable compensation of racking errors in H-frame 3D printers, this paper makes the following original contributions:

¹ An example of this phenomenon can be seen in the following video from the YouTube account by K. Kamal: https://www.youtube.com/watch?v=2_w Wr66bl6Q

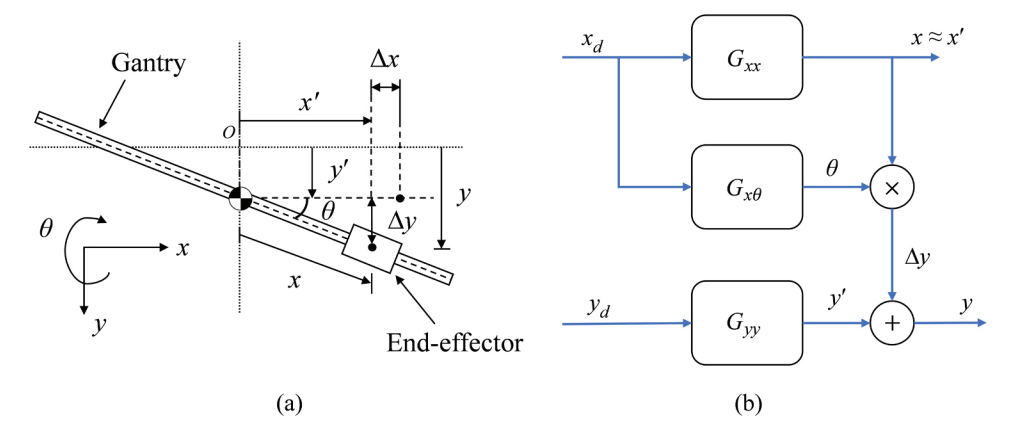


Fig. 2. (a) Kinematic model of parasitic errors created by racking motions of H-frame 3D printers; (b) Dynamic model of H-frame 3D printers including effect of parasitic *y* motions (Δ*y*) created by racking.

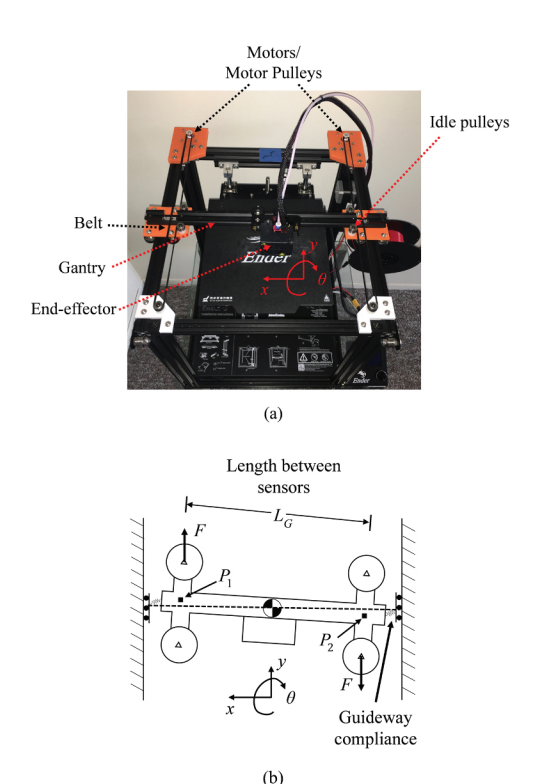


Fig. 3. (a) Designed H-frame 3D printer (retrofitted from the Creality Ender 5 3D printer) used to validate H-frame dynamic model and conduct experiments in Section 4; (b) schematic of racking motion due to the force couple F and guideway compliance denoted by a spring.

- It proposes an extension of the standard FBS controller designed to compensate the coupled LPV racking dynamics of H-frame 3D printers.
- It develops a simplification (i.e., decoupled version) of the designed coupled LPV FBS controller that significantly reduces its computational cost with little to no sacrifice to its racking compensation accuracy.
- 3. It demonstrates the effectiveness and practicality of the developed algorithm in compensating the racking errors through simulations and experiments on an H-frame 3D printer.

The outline of the paper is as follows: Section 2 introduces and validates a model of H-frame racking motion on an H-frame 3D printer. Section 3 gives an overview of the standard FBS method and proposes a

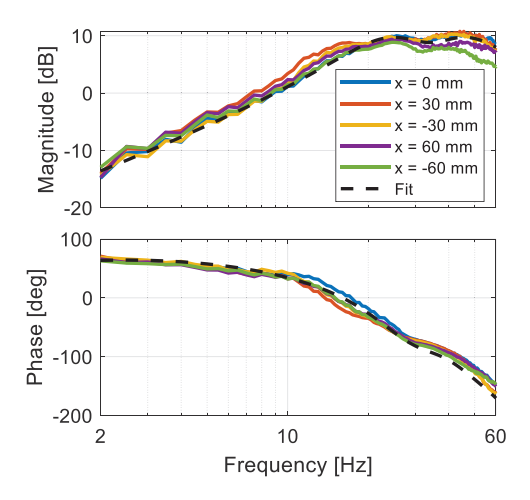


Fig. 4. Frequency response functions from *x*-axis command input to θ output $(G_{x\theta})$ measured with the end-effector positioned at $x=0,\pm 30,$ and ± 60 mm. The differences between the FRFs are small. Therefore, they are modeled by a single FRF shown in dashed lines.

coupled LPV FBS method for compensating racking errors. Section 3 also demonstrates the increased computational cost of the proposed coupled LPV FBS controller, relative to the standard FBS controller, and proposes a simplification that reduces its computational cost with minimal sacrifice to its performance—hence facilitating its practicality. Section 4 presents simulations and experiments on the H-frame 3D printer that demonstrate the effectiveness of the proposed approach, followed by conclusions in Section 5.

2. Model of parasitic racking motion of H-frame

The racking motion of the gantry on the H-frame is caused by a force couple (pure moment) which creates an angular displacement in rotational axis, θ , on the gantry. Let $\{x, y\}$ be the end-effector's output position. It can be decomposed into two portions: $\{x', y'\}$, where x' is the shifted x-axis position with racking errors accounted for, and y' is the desired y-axis position of the end-effector without the racking errors (see Fig. 2(a)), and $\{\Delta x, \Delta y\}$, which are the errors created by racking angle θ as shown in Fig. 2(a). Thus, we have that $x = x' + \Delta x$ and $y = y' + \Delta y$. Using the small angle approximation (i.e., $\cos\theta \approx 1$, $\sin\theta \approx \theta$), $\Delta x \approx 0$ and we can write the x- and y-axis locations as:

$$x \approx x' = x\cos\theta, \ y = y' + x\sin\theta \approx y' + x\theta$$
 (1)

This kinematic model can be used to create a coupled dynamic model including racking, as shown in the block diagram in Fig. 2(b), where

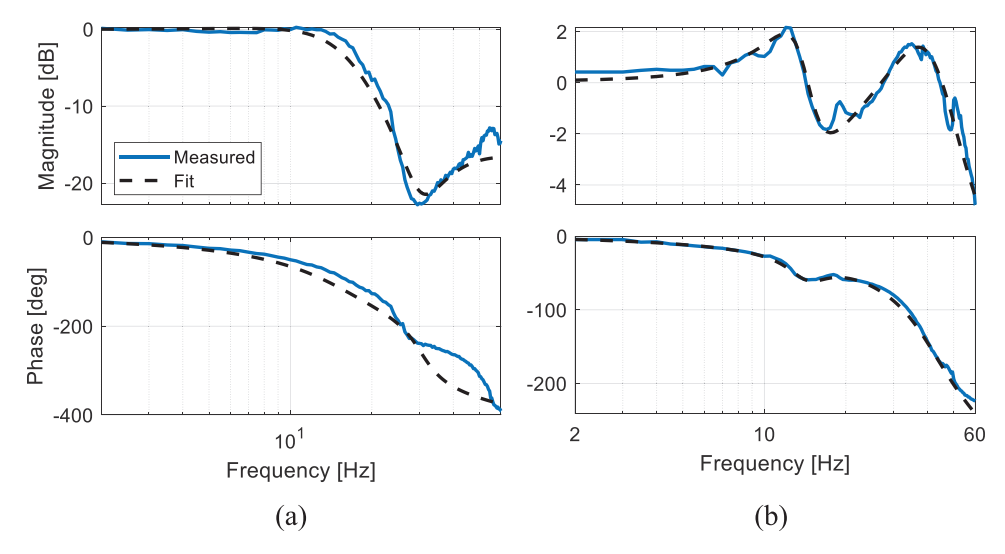


Fig. 5. Measured and curve fit FRFs for (a) G_{xx} and (b) G_{yy} .

Table 1Numerators of fitted transfer functions in Eq. (3).

	b_8	b_7	b_6	b_5	b_4	b_3	b_2	b_1	b_0
$\widehat{G}_{xx}(z)$	-	-	-	-	0.07632	- 0.231	0.236	- 0.0813	$-\ 2.193\times 10^{-13}$
$\widehat{G}_{x\theta}(z)$	4.246	- 29.27	87.51	- 147	149.9	- 92.76	32.26	- 4.865	1.808×10^{-15}
$\widehat{G}_{yy}(z)$	-	-	0.1646	- 0.8951	1.975	- 2.199	1.231	- 0.2764	$-\ 9.173\times 10^{-13}$

 $\{x_d, y_d\}$ represent the desired position of the end-effector. The transfer functions from x_d to x, and y_d to y' are represented by G_{xx} and G_{yy} , respectively, whereas, $G_{x\theta}$ represents the racking contribution (i.e., the transfer function from x_d to θ).

In addition to the small angle approximation, two other assumptions are implied in the model of Fig. 2(b). The first is that the H-frame dynamics can be approximated as linear. Therefore, x, y', and θ can be derived from transfer functions G_{xx} , G_{yy} and $G_{x\theta}$, respectively. This assumption has been found to be reasonable in prior work [5,6,11, 13–16]. The second assumption is that the transfer function $G_{x\theta}$ does not vary as a function of end-effector position, which implies that the inertia of the gantry is not significantly affected by the position of the end-effector as will be validated later in this section.

Remark 2.1. The model shown in Fig. 2(b) is nonlinear because $\Delta y = x\theta$ is generated from the product of two outputs. It can be approximated as linear parameter varying (LPV) by assuming that $x \approx x_d$ when determining Δy . This assumption is reasonable because the tracking errors, $x_d - x$, caused by G_{xx} are typically much smaller than the magnitude of x. Therefore, they have insignificant contributions to Δy . Accordingly, $\Delta y = x_d \theta$ is assumed in the rest of this paper, for the sake of simplicity, resulting in a coupled LPV model for H-frame 3D printers.

The 3D printer shown in Fig. 3(a) is used to validate the H-frame model of Fig. 2. It is fabricated by adapting a Creality Ender 5 3D printer into its H-frame predecessor, the Ender 4. (The Ender 4 was discontinued by Creality, hence was unavailable for purchase.) The designed H-frame configuration is actuated by two NEMA 17 stepper motors via a 2-mm pitch, 6-mm wide, rubber timing belt used for motion transmission. The motors are controlled by Pololu DRV8825 high-current stepper motor drivers configured to give a step resolution of 2 milli-radians per step which is transmitted through a pulley with radius r=5.15 mm to give a

x- and y-axis resolution of 20.6 μ m per step. The motion range of the x and y axes are 280 and 295 mm, respectively. Real-time control of the x, y and z axes and extrusion motors is performed using dSPACE Micro-LabBox (RTI 1202) with stepping frequency of 40 kHz and sampling frequency of 1 kHz. Commands to the printer are generated in MATLAB and sent to the MicroLabBox through a MATLAB Simulink interface.

To validate the model of Fig. 2, sine sweep signals at various frequencies were commanded in the x direction of the printer by applying acceleration commands \ddot{x}_d to the stepper motors and measuring y-axis accelerations at the locations marked P_1 and P_2 in Fig. 3(b) using two ADXL335 three-axis accelerometers. The racking angular acceleration is estimated (based on small angle rotations) as

$$\ddot{\theta} = \frac{\ddot{y}_1 - \ddot{y}_2}{L_G},\tag{2}$$

where \ddot{y}_1 and \ddot{y}_2 are the *y*-axis accelerations measured at P_1 and P_2 at each end of the bridge (Fig. 3(b)) and L_G is the perpendicular distance between P_1 and P_2 . Accordingly, the frequency response function (FRF) $G_{x\theta}$ is computed using \ddot{x}_d as input and $\ddot{\theta}$ as output. Fig. 4 shows $G_{x\theta}$ determined with the end-effector positioned at $x=0,\pm 30$, and ± 60 mm. The discrepancy between the FRFs is small, supporting the assumption that the end-effector position does not significantly influence $G_{x\theta}$. Similarly, G_{xx} and G_{yy} (Fig. 5) are determined by using acceleration commands in the x and y directions, respectively, as inputs and acceleration output measured in the x and y directions with the gantry at x=0 mm.

By curve-fitting the FRFs for $G_{x\theta}$ (Fig. 4), G_{xx} (Fig. 5(a)), and G_{yy} (Fig. 5(b)), discrete transfer functions for each FRF are obtained in the form

$$\widehat{G}(z) = \frac{b_q z^q + b_{q-1} z^{q-1} + \dots + b_1 z + b_0}{z^d + a_{d-1} z^{d-1} + \dots + a_1 z + a_0}$$
(3)

where the $\hat{}$ accent is used to denote a model of the actual dynamics, z is the discrete-time forward shift operator, q and d are the degrees of the

 $^{^2}$ Ender 5 Modified to H-Bot (Ender 4), Thingiverse (2020), https://www.thingiverse.com/thing:4425748.

Table 2
Denominators of fitted transfer functions in Eq. (3).

	a_8	a_7	a_6	a_5	a_4	a_3	a_2	a_1	a_0
$\widehat{G}_{xx}(z)$	-	-	-	-	- 3.577	4.774	- 2.815	0.6175	1.934×10^{-33}
$\widehat{G}_{x\theta}(z)$	- 5.866	14.86	- 21	17.83	- 9.06	2.535	- 0.2987	-2.125×10^{-17}	2.404×10^{-34}
$\widehat{G}_{yy}(z)$	-	-	- 4.813	9.386	- 9.344	4.845	- 1.14	0.06512	

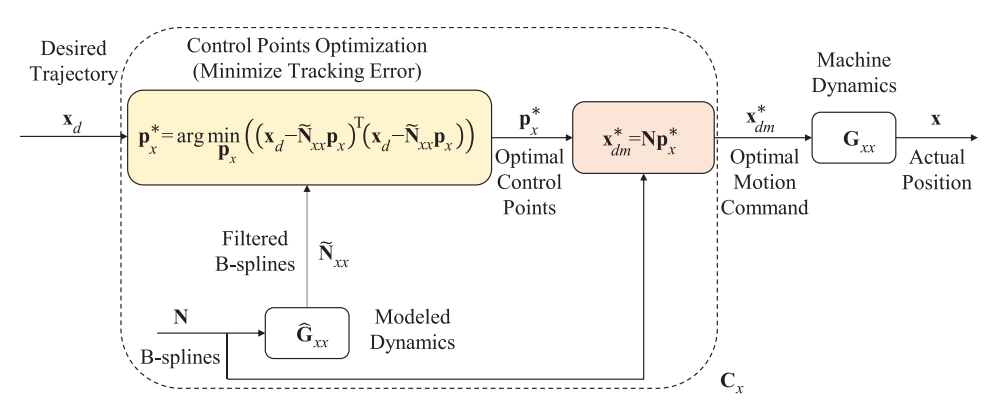


Fig. 6. Block diagram of standard FBS method applied to x-axis of a decoupled multi-axis system.

numerator and denominator polynomials, respectively, and the coefficients of each transfer function are given in Tables 1 and 2. Note that the FRF measured with x at 0 mm is used to fit the transfer function $G_{x\theta}$.

3. Decoupled LTI and proposed coupled LPV filtered B-splines approaches

3.1. Overview of the decoupled LTI FBS approach (i.e., FBS without racking compensation)

Fig. 6 shows the block diagram of the standard filtered B-splines (FBS) approach for the x-axis of a decoupled multi-axis system, i.e., without racking compensation, as introduced in [36]. It controls a decoupled LTI discrete-time system given by G_{xx} , the lifted system (or matrix) representation of transfer function G_{xx} , through a feedforward controller C_x (see Appendix A for details on the lifted system representation).

As shown in Fig. 6, let $\mathbf{x}_d = [x_d(0) \quad x_d(1) \quad \cdots \quad x_d(E)]^{\mathrm{T}}$ represent E+1 discrete time steps of the x-component of a desired trajectory of a multi-axis machine. Assume that the machine has look-ahead capabilities such that the E+1 steps of \mathbf{x}_d are known in advance. Furthermore, assume that the modified but un-optimized motion command $\mathbf{x}_{dm} = [x_{dm}(0) \quad x_{dm}(1) \quad \cdots \quad x_{dm}(E)]^{\mathrm{T}}$ is parameterized using B-splines such that

$$\begin{bmatrix} x_{dm}(0) \\ x_{dm}(1) \\ \vdots \\ x_{dm}(E) \end{bmatrix} = \underbrace{\begin{bmatrix} N_{0,m}(\xi_0) & N_{1,m}(\xi_0) & \cdots & N_{n,m}(\xi_0) \\ N_{0,m}(\xi_1) & N_{1,m}(\xi_1) & \cdots & N_{n,m}(\xi_1) \\ \vdots & \vdots & \ddots & \vdots \\ N_{0,m}(\xi_E) & N_{1,m}(\xi_E) & \cdots & N_{n,m}(\xi_E) \end{bmatrix}}_{N} \underbrace{\begin{bmatrix} p_{x,0} \\ p_{x,1} \\ \vdots \\ p_{x,n} \end{bmatrix}}_{p_{x,n}}$$
(4)

where N is the matrix representation of B-spline basis functions of degree m, \mathbf{p}_x is a vector of n+1 unknown coefficients (or control points), j=0,1,...,n, and $\xi\in[0,1]$ is the spline parameter, representing normalized time, which is discretized to E+1 uniformly spaced points $\xi_0,\xi_1,...,\xi_E$. The real-valued basis functions, $N_{l,m}(\xi)$, are given by [39].

$$N_{j,m}(\xi) = \frac{\xi - g_j}{g_{j+m} - g_j} N_{j,m-1}(\xi) + \frac{g_{j+m+1} - \xi}{g_{j+m+1} - g_{j+1}} N_{j+1,m-1}(\xi),$$

$$N_{j,0} = \begin{cases} 1, & g_j \le \xi \le g_{j+1} \\ 0, & \text{otherwise} \end{cases}$$
(5)

where $\mathbf{g} = [g_0 \ g_1 \ \cdots \ g_{m+n+1}]^T$ is a normalized knot vector defined over [0,1]. For convenience, \mathbf{g} is assumed to be uniformly spaced, i.e.,

$$g_{j} = \begin{cases} 0, & 0 \le j \le m \\ \frac{j-m}{n-m+1}, & m+1 \le j \le n \\ 1, & n+1 \le j \le m+n+1 \end{cases}$$
 (6)

Let x represent the E+1 discrete steps of x, the motion output of the machine's x-axis. Accordingly, based on the definition of \mathbf{x}_{dm} in Eq. (4), x can be written as

$$\mathbf{x} = \widetilde{\mathbf{N}}_{xx} \mathbf{p}_{x} \tag{7}$$

where N_{xx} is the filtered B-spline matrix, acquired by filtering each column of N through G_{xx} (i.e., the matrix product of N and G_{xx}). Using x and x_d , the tracking error can be defined as

$$\mathbf{e}_{x} = \mathbf{x}_{d} - \mathbf{x} = \mathbf{x}_{d} - \widetilde{\mathbf{N}}_{xx}\mathbf{p}_{x}. \tag{8}$$

The optimal control points \mathbf{p}_x^* are calculated by minimizing the square of the L_2 -norm of the tracking error

$$\mathbf{p}_{x}^{*} = \operatorname{argmin}_{\mathbf{p}_{x}} \left(\mathbf{e}_{x}^{\mathsf{T}} \mathbf{e}_{x} \right) = \operatorname{argmin}_{\mathbf{p}_{x}} \left(\left(\mathbf{x}_{d} - \widetilde{\mathbf{N}}_{xx} \mathbf{p}_{x} \right)^{\mathsf{T}} \left(\mathbf{x}_{d} - \widetilde{\mathbf{N}}_{xx} \mathbf{p}_{x} \right) \right)$$
(9)

giving the well-known least squares solution

$$\mathbf{p}_{x}^{*} = \left(\widetilde{\mathbf{N}}_{xx}^{T}\widetilde{\mathbf{N}}_{xx}\right)^{-1}\widetilde{\mathbf{N}}_{xx}^{T}\mathbf{x}_{d} = \widetilde{\mathbf{N}}_{xx}^{\dagger}\mathbf{x}_{d}$$
(10)

where the \dagger in the superscript represents the Moore-Penrose inverse (or pseudoinverse) of the matrix. The result can then be used to calculate the optimized motion command $\mathbf{x}_{dm}^* = \mathbf{N}\mathbf{p}_x^*$. The same procedure is followed to find the optimal control input for other axes, e.g., *y*-axis.

Remark 3.1. The limited-preview version of FBS (LPFBS) [13] relaxes

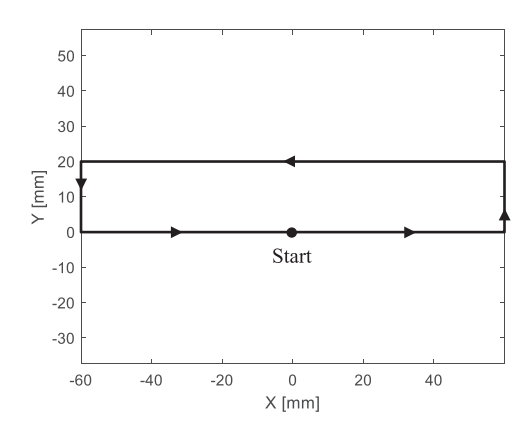


Fig. 7. Rectangular path (with 120 mm length and 20 mm width) used to simulate the time response of the H-frame 3D Printer. The motion command starts at {0,0} and traverses the rectangle in the counterclockwise direction as indicated by the arrows.

the assumption that \mathbf{x}_d is known in advance and instead uses small windows (batches) of \mathbf{x}_d to achieve on-line implementable control. A brief overview of LPFBS is included in Appendix B.

The decoupled LTI implementation of FBS discussed above has two issues due to the introduction of racking. The first is that the motion of the *x*-axis affects the *y*-axis due to racking. Therefore, the *y*-axis cannot be controlled independent of the *x*-axis. The second issue is that the control of the *y*-axis depends on the position of the end-effector on the *x*-axis. Therefore, a coupled LPV FBS approach is needed to include racking dynamics in H-frame 3D printer control.

3.2. Proposed coupled LPV FBS approach (i.e., FBS with racking compensation)

Noting that the racking model from Section 2 can be used to predict the error Δy from Eq. (1), we can use the product of the B-splines matrix N and $G_{x\theta}$ to obtain $\widetilde{N}_{x\theta}$. Therefore, using Eqs. (4) and (7), we have

$$\mathbf{\theta} = \widetilde{\mathbf{N}}_{x\theta} \mathbf{p}_{x} \tag{11}$$

and

$$\Delta \mathbf{y} = \mathbf{D}_{x_d} \widetilde{\mathbf{N}}_{x\theta} \mathbf{p}_x \tag{12}$$

where $\mathbf{D}_{x_d} = \operatorname{diag}(\mathbf{x}_d)$. The tracking error for each axis can then be expressed as

$$\mathbf{e}_{x} = \mathbf{x}_{d} - \mathbf{x} = \mathbf{x}_{d} - \widetilde{\mathbf{N}}_{xx}\mathbf{p}_{x},
\mathbf{e}_{y} = \mathbf{y}_{d} - \mathbf{y} = \mathbf{y}_{d} - (\mathbf{D}_{xd}\widetilde{\mathbf{N}}_{x\theta}\mathbf{p}_{x} + \widetilde{\mathbf{N}}_{yy}\mathbf{p}_{y})$$
(13)

and the optimal control points can be calculated to minimize the squared L_2 -norm of sum of the tracking errors

$$\mathbf{p}^* = \operatorname{arg} min(\mathbf{e}^{\mathsf{T}} \mathbf{e}) \tag{14}$$

where $\mathbf{e} = \begin{bmatrix} \mathbf{e}_x & \mathbf{e}_y \end{bmatrix}^T$, which gives

$$\mathbf{p}^* = \begin{bmatrix} \mathbf{p}_x^* \\ \mathbf{p}_y^* \end{bmatrix} = \begin{bmatrix} \widetilde{\mathbf{N}}_{xx} & \mathbf{0} \\ \mathbf{D}_{x_d} \widetilde{\mathbf{N}}_{x\theta} & \widetilde{\mathbf{N}}_{yy} \end{bmatrix}^{\dagger} \begin{bmatrix} \mathbf{x}_d \\ \mathbf{y}_d \end{bmatrix}. \tag{15}$$

The formulation of the coupled LPV FBS controller in Eq. (15) can be computationally cumbersome during on-line implementation due to the size of the matrix that is inverted. Furthermore, when using LPFBS, since the H-frame is an LPV system, we cannot pre-invert the matrix as is done with LTI FBS, to reduce the computational load (see Appendix B). Therefore, we can decouple the matrices to eliminate the need to compute the pseudoinverse of large matrices during implementation by

computing the control points sequentially: first \mathbf{p}_x^* using Eq. (10), then \mathbf{p}_y^* by rearranging Eq. (13) and considering \mathbf{p}_x^* as a known input

$$\mathbf{p}_{y}^{*} = \widetilde{\mathbf{N}}_{yy}^{\dagger} \left(\mathbf{y}_{d} - \mathbf{D}_{x_{d}} \widetilde{\mathbf{N}}_{x\theta} \mathbf{p}_{x}^{*} \right). \tag{16}$$

Note that in the decoupled approximation using Eqs. (10) and (16), we are inverting the same matrices from LTI FBS, and can pre-invert the matrices for on-line implementation. In Section 3.3 below, we consider the effects of this decoupled approximation on the tracking accuracy and computational complexity of the proposed controller.

Remark 3.2. The LPFBS form of the proposed FBS controller with racking compensation is discussed in Appendix C.

3.3. Tracking accuracy and computational complexity of coupled and decoupled LPV controllers

The system with racking can be expressed in the lifted system representation (see Appendix A) as

$$\mathbf{G} = \begin{bmatrix} \mathbf{G}_{xx} & \mathbf{0} \\ \mathbf{G}_{xy} & \mathbf{G}_{yy} \end{bmatrix} \tag{17}$$

where $G_{xy} = D_{x_d}G_{x\theta}$. The inverse of G is given by

$$\mathbf{G}^{-1} = \begin{bmatrix} \mathbf{G}_{xx}^{-1} & \mathbf{0} \\ -\mathbf{G}_{yy}^{-1} \mathbf{G}_{xy} \mathbf{G}_{xx}^{-1} & \mathbf{G}_{yy}^{-1} \end{bmatrix}$$
 (18)

and the optimal control inputs \mathbf{x}_{dm}^* and \mathbf{y}_{dm}^* are given by

$$\mathbf{x}_{dm}^{*} = \mathbf{G}_{xx}^{-1}\mathbf{x}_{d},
\mathbf{y}_{dm}^{*} = -\mathbf{G}_{yy}^{-1}\mathbf{G}_{xy}\mathbf{G}_{xx}^{-1}\mathbf{x}_{d} + \mathbf{G}_{yy}^{-1}\mathbf{y}_{d}$$
(19)

It can be shown (see [36]) that for n = E, $\widetilde{N}_{xx} = G_{xx}$, $\widetilde{N}_{yy} = G_{yy}$, and the pseudoinversion in Eqs. (10) and (16) become matrix inversion of G_{xx} and G_{yy} , respectively. Therefore, for n = E, the motion command for the decoupled controller, proposed in Section 3.2 can be expressed as

$$\mathbf{x}_{dm}^{*} = \mathbf{G}_{xx}^{-1}\mathbf{x}_{d},
\mathbf{y}_{dm}^{*} = -\mathbf{G}_{yy}^{-1}\mathbf{G}_{xy}\mathbf{G}_{xx}^{-1}\mathbf{x}_{d} + \mathbf{G}_{yy}^{-1}\mathbf{y}_{d}$$
(20)

Note that Eqs. (19) and (20) are identical which shows that the decoupled LPV FBS approach is exactly the same as the inversion of the coupled LPV system when n=E. When n< E, it approximates the coupled LPV system using the FBS approach. Eqs. (10) and (16) are, therefore, another way of approximating the coupled LPV system using the FBS approach.

The computational complexity of the Moore-Penrose inverse, computed using singular value decomposition, is given by $O(lv^2)$ where l and v are the number of rows and columns, respectively, of the matrix to be inverted [40]. We note that the size of the coupled LPV FBS matrix from the Section 3.2 is $2(E+1)\times (n_x+n_y+2)$, where we consider the number of basis functions in the x and y axes independently, and the size of the decoupled matrices are $(E+1)\times (n_x+1)$ and $(E+1)\times (n_y+1)$. Assuming $n=n_x=n_y=E$, the computational complexity of the coupled and decoupled LPV FBS approaches are

$$\begin{array}{lcl} O_c((2E)(2n)^2) & = & O_c((2n)^3) = O_c(8n^3), \\ O_d(En^2 + En^2) & = & O_d(E(n^2 + n^2)) = O_d(En^2) = O_d(n^3) \end{array} \tag{21}$$

where O_c and O_d are the computational orders of the coupled and decoupled approximations, respectively. The expressions in Eq. (21) indicate that the decoupled matrix approximation has much lower computational complexity. The implications of using the decoupled or coupled approximations of the LPV dynamics on racking compensation accuracy and computation time are explored further via simulations in the following section.

Table 3Summary of speed, acceleration, and jerk limits of the baseline and high-speed trajectories.

	Baseline	High-speed	
Speed	60 mm/s	150 mm/s	
Acceleration	$1\times10^3~\text{mm/s}^2$	$1\times 10^4~\text{mm/s}^2$	
Jerk	$5 \times 10^7 \text{ mm/s}^3$	$5 \times 10^7 \text{ mm/s}^3$	

4. Simulations and experiments

4.1. Simulations

Fig. 7 shows the 120-by-20 mm rectangular motion path used for our simulations. It was selected to highlight the racking motion which are prevalent during changes in the *x*-axis acceleration. The trajectory along the path was generated using a jerk-limited motion profile for the two

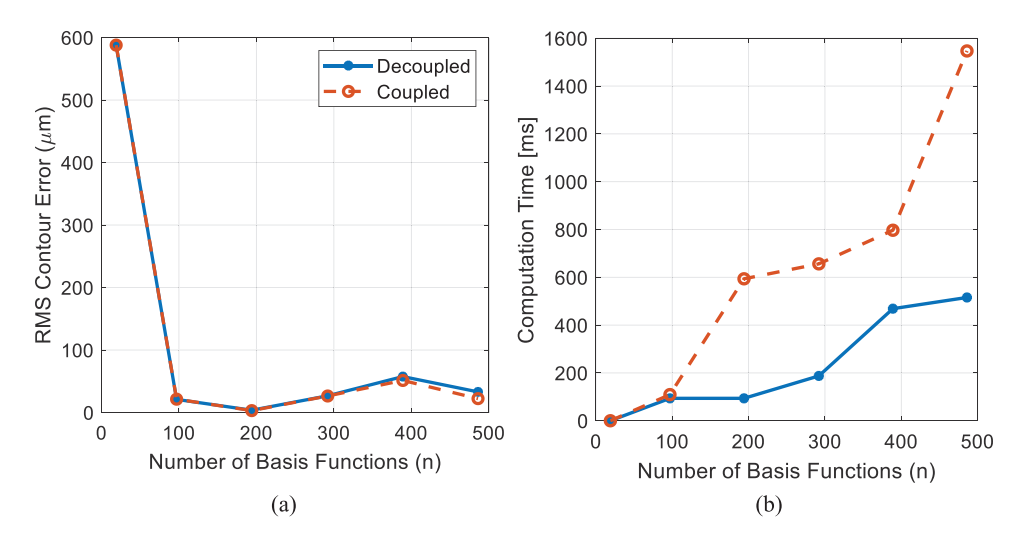


Fig. 8. (a) RMS contour errors and (b) computation times for the simulated time response of the decoupled (solid line) and coupled (dashed line) LPV FBS H-frame controllers as a function of the number of basis functions used to parameterize the trajectory.

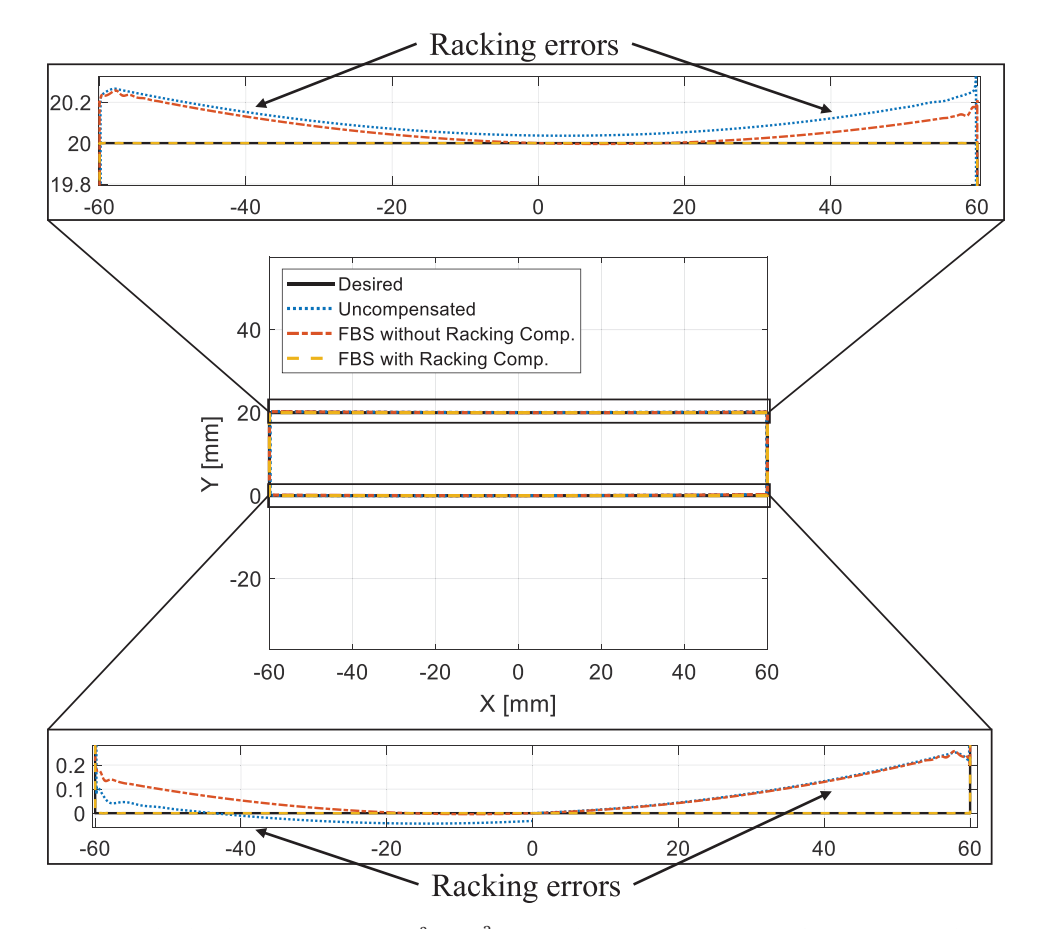


Fig. 9. Simulated output response of the "baseline" ($60 \text{ mm/s}, 1 \times 10^3 \text{ mm/s}^2$) case on the H-frame 3D printer for the uncompensated trajectory (dotted line) as well as the trajectories generated using FBS controllers without racking compensation (dot-dash line) and with racking compensation (dashed line).

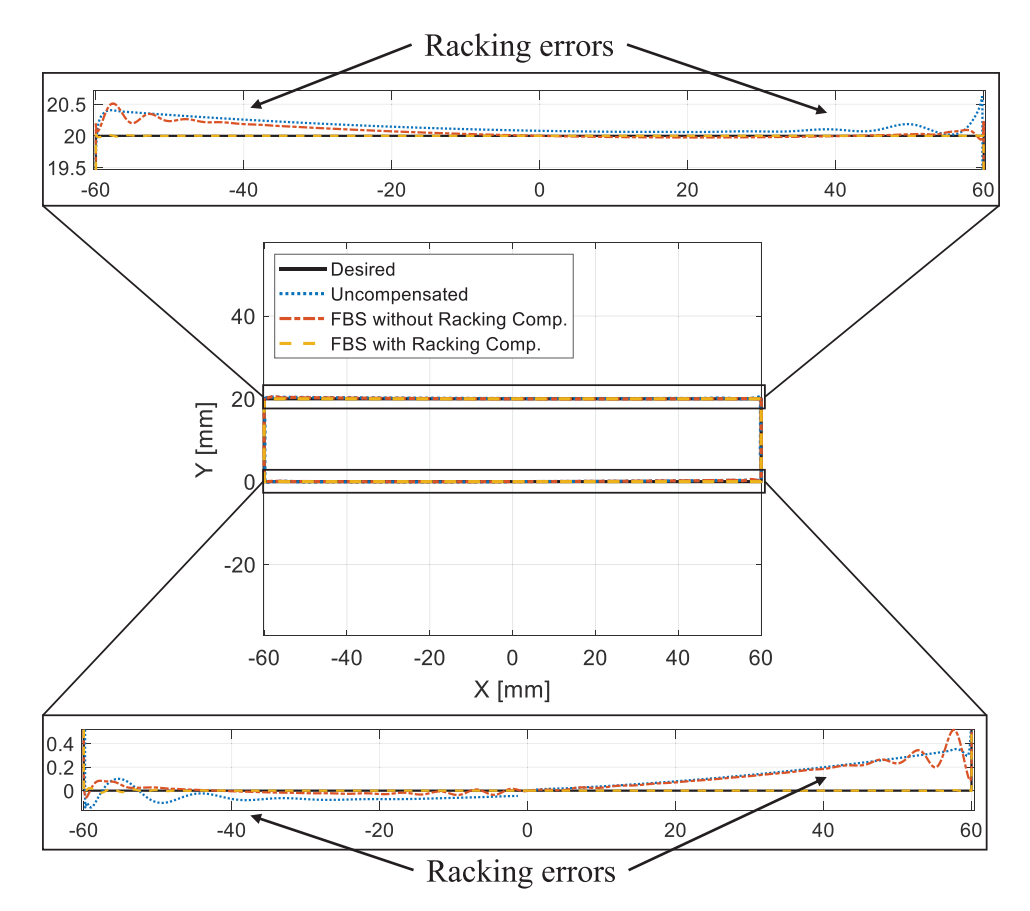


Fig. 10. Simulated output response of the "high-speed" (150 mm/s, 1×10^4 mm/s²) case on the H-frame 3D printer for the uncompensated trajectory (dotted line) as well as the trajectories generated using FBS controllers without racking compensation (dot-dash line) and with racking compensation (dashed line).

Table 4
Root-mean-square (RMS) and maximum contour errors along the baseline (low-speed) and the high-speed cases for all compensation strategies. The FBS with racking compensation controller leads to significant improvements in both the RMS and maximum contour errors for all cases.

Contour error [µm] (RMS / maximum)	Baseline (60 mm/s, 1×10^3 mm/s ²)	$\begin{array}{l} \text{High-speed (150 mm/s,} \\ 1\times10^4 \text{ mm/s}^2) \end{array}$
Uncompensated	127.39 / 341.85	180.01 / 1374.3
FBS without racking compensation	94.02 / 257.84	117.53 / 516.04
FBS with racking compensation	0.16 / 1.92	3.24 / 28.21

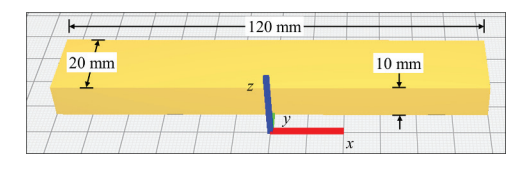


Fig. 11. CAD model of the part in Ultimaker Cura ${\mathbb R}$.

cases presented in Table 3. The first is the baseline case which uses the standard (low) speed and acceleration employed on desktop 3D printers to avoid excessive vibration: 60 mm/s and 1×10^3 mm/s², respectively, with a jerk limit of 5×10^7 mm/s³. The second is a high-speed case, which uses 2.5 times and 10 times the standard speed and acceleration: 150 mm/s and 1×10^4 mm/s², respectively, together with a jerk limit of 5×10^7 mm/s³. The trajectory was sampled at $T_s = 1$ ms, leading to E + 1 = 4970 and 1944 trajectory points for the baseline (low-speed) and

Print parameters for the baseline and high-speed cases of the rectangular block shown in Fig. 11.

Print Parameters	Baseline	High-speed	
Wall speed	60 mm/s	150 mm/s	
Maximum acceleration	$1\times 10^3 \text{ mm/s}^2$	$1\times 10^4 \ mm/s^2$	
Maximum jerk	$5\times 10^7~\text{mm/s}^3$	$5\times 10^7 \ mm/s^3$	
Print material Nozzle diameter	Polylactic acid (PLA) 0.4 mm	Polylactic acid (PLA) 0.4 mm	
Extrusion rate	72 steps / mm	72 steps / mm	
Filament volumetric flow rate	$\begin{array}{l} 1.74 \times 10^{-3} mm^3 / \\ step \end{array}$	$\begin{array}{l} 1.74 \times 10^{-3} \;mm^3/\\ step \end{array}$	
Nozzle temperature	205 °C	205 °C	
Bed temperature	60 °C	60 °C	
Layer height	0.1 mm	0.1 mm	
Wall thickness	0.8 mm	0.8 mm	

high-speed cases, respectively. The model derived and presented in $\frac{2}{2}$ was used as the dynamics to simulate the time response of the H-frame in MATLAB.

4.1.1. Comparison of decoupled and coupled FBS strategies for racking compensation

Before discussing the simulation results, we begin our numerical analysis of the proposed racking compensation algorithm by comparing the tracking accuracy and computational complexity of its decoupled and coupled implementation strategies discussed in Section 3.2. The high-speed case is used for the comparison in this subsection since it is more aggressive and likely to induce racking errors. We compare its

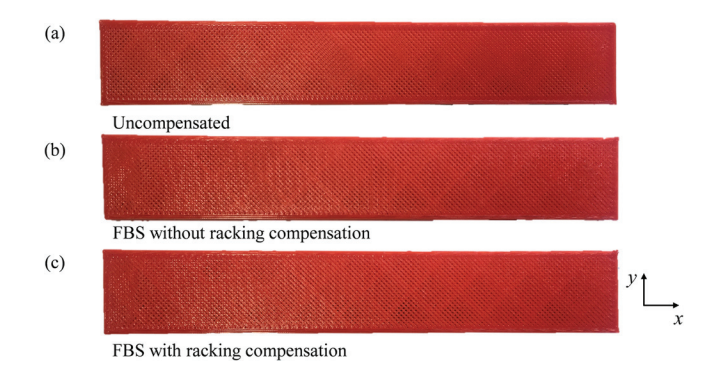


Fig. 12. Examples of the baseline parts printed (a) without any compensation, (b) using FBS without racking compensation, and (c) using FBS with racking compensation. At low speed, print quality differences are hardly distinguishable between the uncompensated and compensated control approaches.

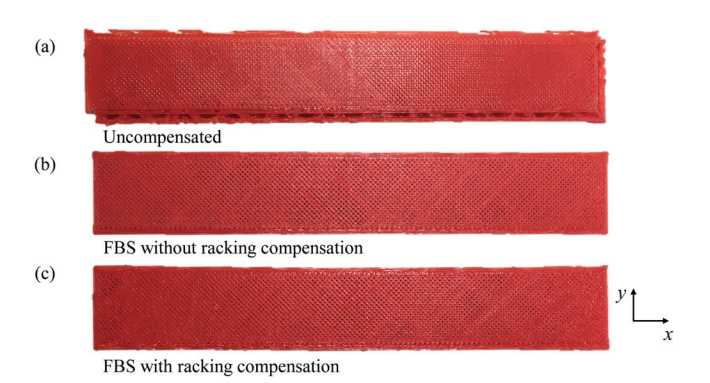


Fig. 13. Examples of the high-speed parts printed (a) without any compensation, (b) using FBS without racking compensation, and (c) using FBS with racking compensation. Layer shifts can be seen in the uncompensated part when compared to the FBS compensated parts. Differences between the FBS without racking compensation and FBS with racking compensation parts can be seen in the enlarged corner view comparison in Fig. 14.

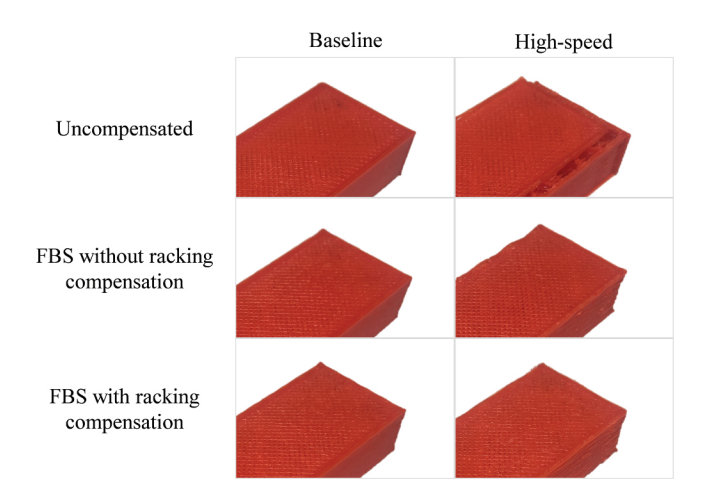


Fig. 14. Enlarged corner view comparison of the baseline and high-speed cases using the uncompensated, FBS without racking compensation, and FBS with racking compensation control approaches. The vibration and racking errors cause layer shifting and waviness along the edge, respectively, for the uncompensated and the FBS without racking compensation approaches applied to the high-speed case. The proposed FBS with racking compensation approach eliminates these errors.

tracking accuracy for each strategy—when n < E—by examining the root-mean-square (RMS) contour errors (i.e., path deviation) of the output trajectory (Fig. 8(a)). The number of basis functions was selected to span fractional values of E, namely n = [0.01, 0.05, 0.1, 0.15, 0.2,0.25]E (rounded to the nearest integer), the B-spline degree was identical for both implementation strategies (m = 5), and the knot vector was defined as in Section 3.1. Consistent with the analysis in Section 3.3, note that the RMS contour error between the two methods is similar for all the n values (Fig. 8(a)), indicating that using the decoupled approach yields similar tracking performance to the coupled approach for a reasonable selection of n. We also validated the computational complexity analysis from Section 3.3 by comparing the computation time of the controller between the two approaches in Fig. 8(b). Note that the coupled approach requires significantly more computation time as nincreases—approximately 3x more time in the worst case. Based on the analysis in Section 3.3 and the results shown in Fig. 8, the decoupled implementation of the coupled LPV FBS controller (i.e., FBS with racking compensation) will be used in all simulations and experiments hereinafter.

4.1.2. Comparison of FBS controller with and without racking compensation

The simulated response of the H-frame machine using the baseline and high-speed cases, controlled with n = 0.1E B-spline basis functions, are shown in Figs. 9 and 10, respectively. Racking errors can be seen at the corners and edges of the rectangle as the trajectory is traversed using the uncompensated case or FBS without racking compensation. Notice also that the severity of the vibration and racking errors are much less with the baseline case compared to the high-speed case. Hence, vibration and racking, when not compensated, limit the achievable speed of H-frame 3D printers if loss of print quality is unacceptable. Racking errors are reduced using the proposed FBS controller with racking compensation, which leads to an output that follows the desired path more accurately for both trajectories. Table 4 shows the RMS and maximum contour errors for both cases compared across the compensation approaches. Here, the maximum contour error indicates whether a part will reach its tolerance specification. Note that, as expected, the baseline has lower maximum contour errors as compared to the highspeed case. For both cases, the uncompensated approach has the highest maximum contour. Comparisons between FBS without racking compensation and FBS with racking compensation show a 99% and 94% reduction in maximum contour error for the baseline and high-speed cases, respectively.

4.2. Experiments

The same rectangular profile used in Section 4.1 was extruded to a height of 10 mm and printed on the H-frame 3D printer. The CAD model of the rectangular prism can be seen in Fig. 11. The G-code for the trajectory was generated using the open-source Ultimaker Cura® software. As with the simulations, two cases were considered in experiments: the baseline and high-speed cases, with wall speed, maximum acceleration and maximum jerk values reported in Table 5, along with other print parameters. To ensure adhesion to the bed, the first four layers in both cases were printed at a speed of 20 mm/s.

Figs. 12 and 13 compare the rectangular block printed for the baseline and high-speed cases, respectively, using no compensation, FBS without racking compensation and the proposed FBS with racking compensation. The limited-preview version of FBS, i.e., LPFBS, was used in both FBS cases, with parameters $n_{up}=11, n_C=22, L_C=220, m=5, \ {\rm and}\ L=20$ (see Appendix B and C for more details). As can be seen from Fig. 12(a), the baseline case without compensation yields high-quality prints (in terms of vibration and racking) which are hardly distinguishable from those with compensation (Fig. 12(b) and (c)). This observation highlights why printers with vibration and racking problems often yield excellent print quality at low speeds (albeit at the cost of

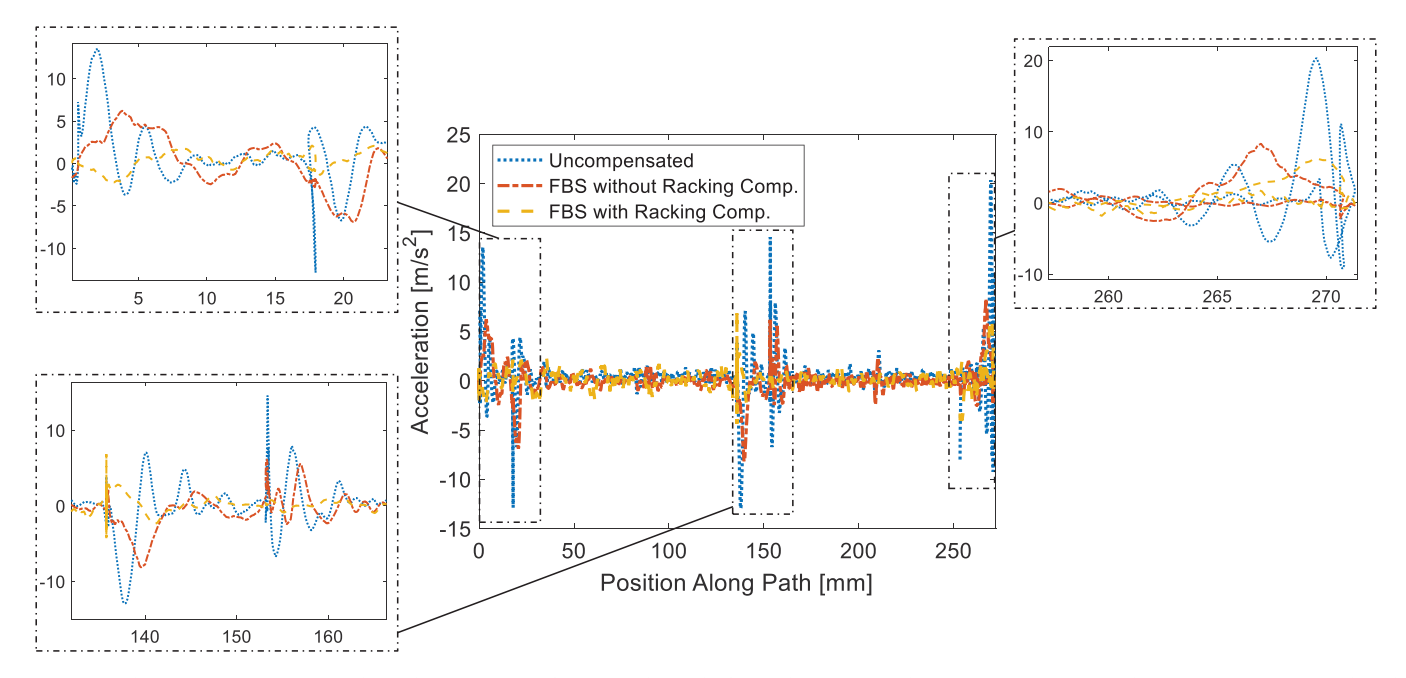


Fig. 15. Acceleration measurements of the racking motion of the gantry during high-speed printing on the H-frame 3D printer without any compensation (dotted line), using FBS without racking compensation (dot-dash line), and using FBS with racking compensation (dashed line). The positions of high acceleration are highlighted.

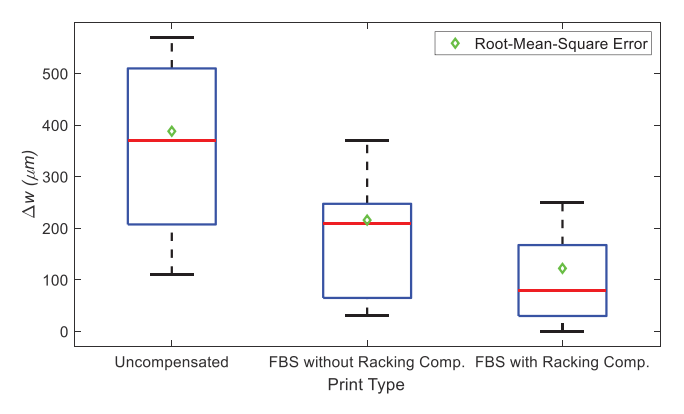


Fig. 16. Box-and-whisker plot of measured absolute width error, Δw , of printed parts compared to the desired width of 20 mm for each of the compensation strategies applied to the high-speed case: (1) no compensation, (2) FBS without racking compensation, and (3) FBS with racking compensation. The red horizontal lines represent the median of Δw , which is overlaid with root-mean-square width error, Δw_{rms} (diamonds).

productivity). However, as seen from Fig. 13(a), the situation is different with the high-speed case. The part printed without compensation suffered from printing layer shifts during the printing process (as also observed in [13]). The FBS approach without racking compensation (Fig. 13(b)) provides sufficient compensation to remove the layer shifts from the printed part. However, the quality of the part is still degraded relative to the baseline case, as is evident from the waviness along the edges of the part in Fig. 14 (that were also see in the simulation results of Fig. 10). The proposed FBS with racking compensation rectifies both the layer shifting and waviness due to racking leading much better print quality (see Fig. 14).

To quantify the improvements to the high-speed case due to the proposed approach, the acceleration of the gantry was measured using the ADXL335 accelerometers positioned at P_1 and P_2 in Fig. 3(b) during the print motion of the high-speed case. This measurement can be thought of as a proxy for the position errors since the 3D printer is not

equipped with position sensors on the gantry or nozzle. Fig. 15 shows the acceleration measurements for one side of the gantry as a function of the position along the rectangular path of one layer during the print motion for (1) an uncompensated part, (2) a part printed using FBS without racking compensation and (3) a part printed using FBS with racking compensation. (Note that the path of the measurements starts at the $\{x, y\}$ position of $\{60, 0\}$ mm instead of $\{0, 0\}$ as in Fig. 7.) The RMS acceleration of the gantry during the three high-acceleration portions highlighted in Fig. 15 are 3.63, 4.25, and 5.61 m/s² for the uncompensated approach, 2.41, 2.62, and 2.63 m/s² for FBS without racking compensation, and 1.10, 1.04, and 2.21 m/s² for FBS with racking compensation. These data indicate that the additional acceleration created by racking in the uncompensated trajectory and the trajectory using FBS without racking compensation are significantly reduced by the proposed racking compensation approach, leading to greater positional accuracy.

To further quantify how the racking errors affect the final component for the high-speed case, we printed 15 copies of the rectangular prism using the three different compensation approaches (5 copies for each). The width, w, of each of the 15 printed parts was measured at the left, middle, and right side using Husky digital calipers (model# 1467 H, 10 μ m resolution) and compared to the desired width of $w_d = 20$ mm. Fig. 16 shows a box-and-whisker plot of the absolute value of the width error $(\Delta w = |w_d - w|)$ overlaid with the RMS width error, Δw_{rms} . The proposed FBS controller with racking compensation improved the median Δw by 61% when compared to FBS without racking compensation, from 210 μ m to 80 μ m, and by 78% when compared to no compensation from 370 μ m to 80 μ m. The proposed controller also improved Δw_{rms} by 43% (216 μ m to 122 μ m) and 68% (388 μ m to 122 μ m) compared to FBS without racking compensation and no compensation, respectively. Note that even though print quality depends on several factors (e.g., material, extrusion rate, extrusion temperature, etc.), in the comparisons discussed above for the baseline and high-speed cases, all other factors are maintained constant except for the compensation approach. Therefore, the differences in print quality are primarily due to the effects of compensation approach.

5. Conclusion

H-frame 3D printer architectures hold potential to achieve higher speeds and improved dynamic performance compared to traditional serial stack 3D printers due to their use of stationary motors. However, these benefits come at the cost of racking errors, caused by parasitic torsional motions, which limit their static and dynamic accuracy. This paper proposes a purely software-based approach for compensating racking errors on H-frame 3D printers using the filtered B-splines (FBS) feedforward controller that has been used to improve the performance of 3D printers in prior work [13,15,19]. However, to compensate racking errors, the proposed FBS controller is designed to address coupled linear parameter varying dynamics rather than decoupled linear time invariant dynamics addressed in prior work. A decoupled approximation of the proposed coupled FBS controller, which significantly reduces computational complexity with little or no sacrifice to error compensation accuracy, is developed and validated analytically and numerically. The decoupled FBS controller with racking compensation is benchmarked in simulation and experiments on an H-frame 3D printer against the standard FBS controller without racking compensation. Using the proposed approach, racking errors are significantly reduced and a 43% improvement in the shape accuracy of a high-speed printed part is observed in experiments compared to the standard FBS controller.

A major practical benefit of the proposed software-based approach for racking error compensation is that it reduces racking errors without requiring mechanical modification of a 3D printer. Hence, it can be applied to existing H-frame 3D printers. It can also be used to augment other mechanical or software-based approaches for addressing racking errors, like the use of stiffer guideways, counterweights, dampers, and

feedback controllers. This paper shows the potential of software-based compensation approaches to improve the dynamic performance of parallel-axis motion-stage architectures (often used on 3D printers). Future work will explore the application of the FBS approach to other parallel-axis motion-stage architectures that suffer from coupled dynamics and parasitic errors, like delta 3D printers.

CRediT authorship contribution statement

The authors certify that we have all have seen and approved the final version of the manuscript being submitted. We warrant that the article is our original work, has not received prior publication and is not under consideration for publication elsewhere.

Declaration of Competing Interest

The authors declare the following financial interests/personal relationships which may be considered as potential competing interests: A company founded by C.E. Okwudire holds a commercial license for the filtered B spline (FBS) algorithm.

Acknowledgements

This work was supported in part by the National Science Foundation [grants numbers DGE 1256260 and CMMI 1825133] and the National Aeronautics and Space Administration (NASA), under award number 80NSSC20M0124, Michigan Space Grant Consortium (MSGC). The authors would also like to thank Mr. Chandler Harris for his assistance in retrofitting the H-frame 3D printer used in the experiments.

Appendix A. Lifted system representation of a digital filter

Consider filter *p*, input signal *u*, and output signal *y* defined as:

$$p = \{p_{-2} p_{-1} p_0 p_1 p_2\}$$

$$u = \{u_0 u_1 u_2\},$$

$$y = \{y_0 y_1 y_1\}$$
(22)

Signals *y* and *u* and filter *p* are related by the convolution operator as follows:

$$y = u * p \tag{23}$$

From Eqs. (22) and (23)

$$y_0 = p_0 u_0 + p_{-1} u_1 + p_{-2} u_2$$

$$y_1 = p_1 u_0 + p_0 u_1 + p_{-1} u_2,$$

$$y_2 = p_2 u_0 + p_1 u_1 + p_0 u_2$$
(24)

This can be expressed in matrix form as

$$\begin{bmatrix} y_0 \\ y_1 \\ y_2 \end{bmatrix} = \begin{bmatrix} p_0 & p_{-1} & p_{-2} \\ p_1 & p_0 & p_{-1} \\ p_2 & p_1 & p_0 \end{bmatrix} \begin{bmatrix} u_0 \\ u_1 \\ u_2 \end{bmatrix}$$
 (25)

Note that the main diagonal element (p_0) represents the influence of the current input on the current output; the first upper diagonal element (p_{-1}) represents the influence of the succeeding input on the current output and the second upper diagonal element (p_{-2}) represents the influence of the second succeeding input on the current output. Similarly, the first (p_1) and second lower (p_2) elements represent the influence of the first and second preceding inputs on the current output, respectively. Hence, the discrete time (or z) transform of p obtained from Eq. (25) is given by

$$p_2 z^{-2} + p_1 z^{-1} + p_0 z^0 + p_{-1} z^1 + p_{-2} z^2$$
(26)

which is in accordance with the time-domain definition given in Eq. (22).

Appendix B. Standard implementation of limited-preview filtered B-splines approach

This appendix presents a brief discussion of the limited-preview filtered B-splines approach. For more details, interested readers can refer to [13]. The limited-preview FBS approach aims to generate optimal feedforward control inputs in sequential windows (batches) of the desired trajectory \mathbf{x}_d . Since \mathbf{x}_d is not assumed to be fully known a priori, an un-normalized and open-ended knot vector is used and defined as

$$\overline{g}_j = \begin{cases} 0, & 0 \le j \le m \\ (j-m)LT_s, & j \le m+1 \end{cases}$$

$$(27)$$

where j and m are as defined in Section 3, and $L \ge 1$ represents the uniform spacing of the knot vector elements as an integer multiple of the sampling time T_s . With the un-normalized knot vector, $N_{j,m}$ is expressed as a function of time t by replacing ξ with t and g_j with \overline{g}_j in Eq. (5), and the function is sampled at $t_k = kT_s$ to formulate N as in Eq. (4). The tracking problem is solved in batches as

$$\overline{\mathbf{e}} = \mathbf{x}_{d} - \overline{\mathbf{N}} \overline{\mathbf{p}} \Leftrightarrow \begin{bmatrix} \overline{\mathbf{e}}_{\mathrm{P}} \\ \overline{\mathbf{e}}_{\mathrm{C}} \\ \overline{\mathbf{e}}_{\mathrm{F}} \end{bmatrix} = \begin{bmatrix} \mathbf{x}_{d,\mathrm{P}} \\ \mathbf{x}_{d,\mathrm{C}} \\ \mathbf{x}_{d,\mathrm{F}} \end{bmatrix} - \begin{bmatrix} \overline{\mathbf{N}}_{\mathrm{P}} & \mathbf{0} & \mathbf{0} \\ \overline{\mathbf{N}}_{\mathrm{PC}} & \overline{\mathbf{N}}_{\mathrm{C}} & \mathbf{0} \\ \mathbf{0} & \overline{\mathbf{N}}_{\mathrm{CF}} & \overline{\mathbf{N}}_{\mathrm{F}} \end{bmatrix} \begin{bmatrix} \overline{\mathbf{p}}_{\mathrm{P}} \\ \overline{\mathbf{p}}_{\mathrm{C}} \\ \overline{\mathbf{p}}_{\mathrm{F}} \end{bmatrix}$$

$$(28)$$

where subscripts 'P', 'C', and 'F' denote the past, current, and future batches, respectively, and the bar on the matrices and vectors indicates that the impulse response of the transfer function used for filtering the B-splines is truncated. Using local least squares, the optimal coefficients of the current batch can be computed as

$$\overline{\mathbf{p}}_{C} = \left(\overline{\mathbf{N}}_{C}^{T} \overline{\mathbf{N}}_{C}\right)^{-1} \overline{\mathbf{N}}_{C}^{T} \left(\mathbf{x}_{d,C} - \overline{\mathbf{N}}_{PC} \overline{\mathbf{p}}_{P}\right)$$
(29)

where \overline{p}_P denotes the coefficients calculated in the last batch. Note that the information from the future batch is not considered while calculating coefficients for the current batch. Also note that the matrix \overline{N}_C can be pre-inverted once and applied to all batches.

The dimensions of the current window are defined by L_C and n_C , where L_C is the number of trajectory points considered in the current batch and n_C is the number of B-spline coefficients. Note that although n_C coefficients are computed, only n_{up} are updated in each window (see Fig. B.1).

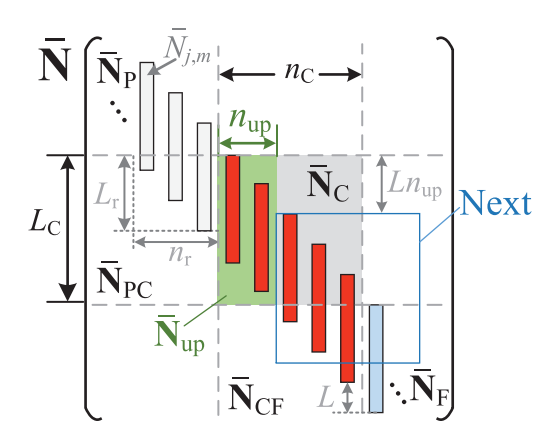


Fig. B1. Illustration for LPFBS.

Appendix C. Limited-preview filtered B-splines for coupled LPV controller

From Eqs. (16) and (28), a natural extension of LPFBS can be made for the coupled LPV system. The tracking error is given by

$$\overline{\mathbf{e}} = \mathbf{r}_{d} - \overline{\mathbf{N}}_{r} \overline{\mathbf{p}}_{r} \Leftrightarrow \begin{bmatrix} \overline{\mathbf{e}}_{r,P} \\ \overline{\mathbf{e}}_{r,C} \\ \overline{\mathbf{e}}_{r,F} \end{bmatrix} = \begin{bmatrix} \mathbf{r}_{d,P} \\ \mathbf{r}_{d,C} \\ \mathbf{r}_{d,F} \end{bmatrix} - \begin{bmatrix} \overline{\mathbf{N}}_{r,P} & \mathbf{0} & \mathbf{0} \\ \overline{\mathbf{N}}_{r,PC} & \overline{\mathbf{N}}_{r,C} & \mathbf{0} \\ \mathbf{0} & \overline{\mathbf{N}}_{r,CF} & \overline{\mathbf{N}}_{r,F} \end{bmatrix} \begin{bmatrix} \overline{\mathbf{p}}_{r,P} \\ \overline{\mathbf{p}}_{r,C} \\ \overline{\mathbf{p}}_{r,F} \end{bmatrix}$$

$$(30)$$

where $\mathbf{r}_d = [\mathbf{x}_d \ \mathbf{y}_d]^T$, and the subscript r denotes matrices and vectors related to \mathbf{r}_d . Expanding the tracking error of the current batch as

$$\overline{\mathbf{e}}_{r,C} = \begin{bmatrix} \mathbf{x}_{d,C} \\ \mathbf{y}_{d,C} \end{bmatrix} - \begin{bmatrix} \overline{\mathbf{N}}_{x,PC} & \mathbf{0} & \overline{\mathbf{N}}_{x,C} & \mathbf{0} \\ \mathbf{D}_{\mathbf{x}_{d,PC}} \overline{\mathbf{N}}_{x\theta,PC} & \overline{\mathbf{N}}_{x\theta,C} & \overline{\mathbf{N}}_{y,C} \end{bmatrix} \begin{bmatrix} \overline{\mathbf{p}}_{x,P} \\ \overline{\mathbf{p}}_{y,P} \\ \overline{\mathbf{p}}_{x,C} \\ \overline{\mathbf{p}}_{y,C} \end{bmatrix}, \tag{31}$$

the coefficients for the current batch are calculated as

$$\begin{bmatrix} \overline{\mathbf{p}}_{x,C} \\ \overline{\mathbf{p}}_{y,C} \end{bmatrix} = \begin{bmatrix} \overline{\mathbf{N}}_{x,C} & \mathbf{0} \\ \mathbf{D}_{x_{d,C}} \overline{\mathbf{N}}_{x\theta,C} & \overline{\mathbf{N}}_{y,C} \end{bmatrix}^{\dagger} \begin{pmatrix} \begin{bmatrix} \mathbf{x}_{d,C} \\ \mathbf{y}_{d,C} \end{bmatrix} - \begin{bmatrix} \overline{\mathbf{N}}_{x,PC} & \mathbf{0} \\ \mathbf{D}_{x_{d,PC}} \overline{\mathbf{N}}_{x\theta,PC} & \overline{\mathbf{N}}_{y,PC} \end{bmatrix} \begin{bmatrix} \overline{\mathbf{p}}_{x,P} \\ \overline{\mathbf{p}}_{y,P} \end{bmatrix} \end{pmatrix}. \tag{32}$$

The coefficients in the decoupled approximation can be calculated sequentially. First, we calculate $\overline{p}_{x,C}$ using \overline{p}_{C} in Eq. (29) applied to the *x*-axis, and use the obtained coefficients to obtain $\overline{p}_{y,C}$ as

(33)

$$\overline{\mathbf{p}}_{\mathrm{v.C}} = \overline{\mathbf{N}}_{\mathrm{v.C}}^{\dagger} (\mathbf{y}_{d.\mathrm{C}} - (\mathbf{D}_{x_{d,\mathrm{PC}}} \overline{\mathbf{N}}_{x\theta,\mathrm{PC}} \overline{\mathbf{p}}_{x,\mathrm{P}} + \mathbf{D}_{x_{d,\mathrm{C}}} \overline{\mathbf{N}}_{x\theta,\mathrm{C}} \overline{\mathbf{p}}_{x,\mathrm{C}}) - \overline{\mathbf{N}}_{\mathrm{y,PC}} \overline{\mathbf{p}}_{\mathrm{y,P}}).$$

References

- Sculpteo, Inc, The state of 3D printing: the data you need to understand the 3D printing world and build your 3D printing strategy, San Francisco, CA, 2021.
- [2] J.W. Comb, W.J. Swanson, J.L. Crotty, Gantry assembly for use in additive manufacturing system. U.S. Patent Application No. 20130078073(A1). Washington, DC: U.S. Patent and Trademark Office 2011.
- [3] R. Clavel, Delta: a fast robot with parallel geometry, 18th Int. Symposium on Industrial Robots, pp. 91–100, 1988.
- [4] A.R. Avdeev, A.A. Shvets, I.S. Torubarov, Investigation of kinematics of 3D printer print head moving systems, in: Proceeding of the 5th Int. Conf. on Industrial Engineering, pp. 461–471 (2020). https://doi.org/10.1007/978-3-030-22041 -9 50
- [5] K.S. Sollmann, M.K. Jouaneh, D. Lavender, Dynamic modeling of a two-axis, parallel, H-frame-type XY positioning system, IEEE/ASME Trans, Mechatronics 15 (2) (2010) 280–290, https://doi.org/10.1109/TMECH.2009.2020823.
- [6] G. Phanomchoeng, R. Chancharoen, Adaptive gain control for a two-axis, H-Frame-type, positioning system, Eng. J. 21 (3) (2017) 223–234, https://doi.org/10.4186/aii2017.21.3.232
- [7] Stratasys Inc. 3D printers, http://www.stratasys.com/3d-printers, (accessed 27 June 2020).
- [8] MakerBot 3D printers, https://www.makerbot.com/3d-printers/, (accessed 27 June 2020).
- [9] Creality Ender 4: Review the specs, All3DP (2019), https://all3dp.com/1/creality-ender-4-3d-printer-review/, (accessed 27 June 2020).
- [10] J. Go, A.J. Hart, Fast desktop-scale extrusion additive manufacturing, Addit. Manufac. 18 (2017) 276–284, https://doi.org/10.1016/j.addma.2017.10.016.
- [11] K.S. Sollmann, Modeling, Simulation, and Control of A Belt-driven, Parallel H-frame Type Two Axes Positioning System, University of Rhode Island, South Kingstown, Rhode Island, USA, 2007. https://digitalcommons.uri.edu/thepse/607/
- [12] D. Miu, Mechatronics, Springer-Verlag, New York, 1993.
- [13] M. Duan, D. Yoon, C.E. Okwudire, A limited-preview filtered B-spline approach to tracking control—with application to vibration-induced error compensation of a 3D printer, Mechatronics 56 (2018) 287–296, https://doi.org/10.1016/j. mechatronics.2017.09.002.
- [14] K.S. Ramani, N. Edoimioya, C.E. Okwudire, A robust filtered basis functions approach for feedforward tracking control – with application to a vibration-prone 3D printer, IEEE/ASME Trans. Mechatron. 25 (5) (2020) 2556–2564, https://doi. org/10.1109/TMECH.2020.2983680.
- [15] C.E. Okwudire, S. Huggi, S. Supe, C. Huang, B. Zeng, Low-level control of 3D printers from the cloud: a step toward 3D printer control as a service, Inventions 3 (56) (2018), https://doi.org/10.3390/inventions3030056.
- [16] H. Kim, C.E. Okwudire, Simultaneous servo error pre-compensation and feedrate optimization with tolerance constraints using linear programming, Int. J. Adv. Manuf. Technol. 109 (2020) 809–821, https://doi.org/10.1007/s00170-020-05651.
- [17] P. Chesser, B. Post, A. Roschli, C. Carnal, R. Lind, M. Borish, L. Love, Extrusion control for high quality printing on Big Area Additive Manufacturing (BAAM) systems, Addit. Manuf. 28 (2019) 445–455, https://doi.org/10.1016/j. addma.2019.05.020.
- [18] D.S. Ertay, A. Yuen, Y. Altintas, Synchronized material deposition rate control with path velocity on fused filament fabrication machines, Addit. Manuf. 19 (2018) 205–213, https://doi.org/10.1016/j.addma.2017.05.011.
- [19] Q. Wang, P.P. Michaleris, A.R. Nassar, J.E. Irwin, Y. Ren, C.B. Stutzman, Model-based feedforward control of laser powder bed fusion additive manufacturing, Addit. Manuf. 31 (2020), 100985, https://doi.org/10.1016/j.addma.2019.100985.
- [20] C.L. Druzgalski, A. Ashby, G. Guss, W.E. King, T.T. Roehling, M.J. Matthews, Process optimization of complex geometries using feed forward control for laser powder bed fusion additive manufacturing, Addit. Manuf. 34 (2020), 101169, https://doi.org/10.1016/j.addma.2020.101169.

- [21] S. Moralejo, X. Penaranda, S. Nieto, A. Barrios, I. Arrizubieta, I. Tabernero, J. Figueras, A feedforward controller for tuning laser cladding melt pool geometry in real time, Int. J. Adv. Manuf. Technol. 89 (2017) 821–831, https://doi.org/ 10.1007/s00170-016-9138-7.
- [22] K. Erkorkmaz, Y. Altintas, High speed CNC system design. Part I: jerk limited trajectory generation and quintic spline interpolation, Int. J. Mach. Tools Manuf. 41 (9) (2001) 1323–1345, https://doi.org/10.1016/S0890-6955(01)00002-5.
- [23] C.S. Chen, A.C. Lee, Design of acceleration/deceleration profiles in motion control based on digital FIR filters, Int. J. Mach. Tools Manuf. 38 (7) (1998) 799–825, https://doi.org/10.1016/S0890-6955(97)00065-5.
- [24] J.H. Chen, S.S. Yeh, J.T. Sun, An S-curve acceleration/deceleration design for CNC machine tools using quintic feedrate function, Comput. -Aided Des. Appl. 8 (4) (2011) 583–592, https://doi.org/10.3722/cadaps.2011.583-592.
- [25] N. Singer, W. Singhose, W. Seering, Comparison of filtering methods for reducing residual vibration, Eur. J. Control 5 (1999) 208–218, https://doi.org/10.1016/ S0947-3580(99)70155-X.
- [26] P.J. Barre, R. Bearee, P. Borne, E. Dumetz, Influence of a jerk controlled movement law on the vibratory behavior of high-dynamics systems, J. Intel. Rob. Syst. 42 (3) (2005) 275–293, https://doi.org/10.1007/s10846-004-4002-7.
- [27] N.C. Singer, W.P. Seering, Design and comparison of command shaping methods for controlling residual vibration, Proc. IEEE Int. Conf. Robot. Autom. (1989) 888–893, https://doi.org/10.1109/ROBOT.1989.100094.
- [28] W. Singhose, Command shaping for flexible systems: a review of the first 50 years, Int. J. Precis. Eng. Manuf. 10 (4) (2009) 153–168, https://doi.org/10.1007/ s12541-009-0084-2.
- [29] B. Sencer, A. Dumanli, Y. Yamada, Spline interpolation with optimal frequency spectrum for vibration avoidance, CIRP Ann. Manuf. Technol. 67 (1) (2018) 377–380, https://doi.org/10.1016/j.cirp.2018.03.002.
- [30] Y. Altintas, M.R. Khoshdarregi, Contour error control of CNC machine tools with vibration avoidance, CIRP Ann. Manuf. Technol. 61 (1) (2012) 335–338, https:// doi.org/10.1016/j.cirp.2012.03.132.
- [31] J. van Zundert, T. Oomen, On inversion-based approaches for feedforward and ILC, Mechatronics 50 (2018) 282–291, https://doi.org/10.1016/j. mechatronics 2017 09 010
- [32] K.S. Ramani, N. Edoimioya, C.E. Okwudire, A robust filtered basis functions approach for feedforward tracking control – with application to a vibration-prone 3D printer, IEEE/ASME Trans. Mechatron. 25 (5) (2020) 2556–2564, https://doi. org/10.1109/TMECH.2020.2983680.
- [33] B.P. Rigney, L.Y. Pao, D.A. Lawrence, Nonminimum phase dynamic inversion for settle time applications, IEEE Trans. Control Syst. Technol. 17 (5) (2009) 989–1005, https://doi.org/10.1109/TCST.2008.2002035.
- [34] G.M. Clayton, S. Tien, K.K. Leang, Q. Zou, S. Devasia, A review of feedforward control approaches in nanopositioning for high-speed SPM, J. Dyn. Syst. Meas. Control 131 (6) (2009), 061101, https://doi.org/10.1115/1.4000158.
- [35] C.E. Okwudire, K.S. Ramani, M. Duan, A trajectory optimization method for improved tracking of motion commands using CNC machines that experience unwanted vibration, CIRP Ann. Manuf. Technol. 65 (1) (2016) 373–376, https:// doi.org/10.1016/j.cirp.2016.04.100.
- [36] K.S. Ramani, M. Duan, C.E. Okwudire, A.G. Ulsoy, Tracking control of linear time-invariant nonminimum phase systems using filtered basis functions, J. Dyn. Syst. Meas. Control 139 (1) (2017), 011001, https://doi.org/10.1016/j.cirp.2016.04.100.
- [37] M. Duan, K.S. Ramani, C.E. Okwudire, Tracking control of non-minimum phase systems using filtered basis functions: a NURBS-based approach, ASME Dyn. Syst. Control Conf. (2015), https://doi.org/10.1016/j.cirp.2016.04.100.
- [38] Y. Kasemsinsup, R. Romagnoli, M. Heertjes, S. Weiland, H. Butler, Reference-tracking feedforward control design for linear dynamical systems through signal decomposition, Am. Control Conf. (2017) 2387–2392, https://doi.org/10.23919/ACC.2017.7963310.
- [39] L. Piegl, W. Tiller, The NURBS Book, Springer, Berlin, Heidelberg, 1995.
- [40] G.H. Golub, C.F. Van Loan, Matrix Computations, fourth ed., The Johns Hopkins University Press, 2013.